3D Printing of Lead-Free Piezoelectric Ultrasound Transducers

Ammu, Satya K.; Chen, Xianfeng; Ulcay, Derin Goulart; Sharma, Saurav; Alijani, Farbod; Steeneken, Peter G.; Groen, Pim; Masania, Kunal

DOI
10.1002/admt.202400858

Publication date
2024

Document Version
Final published version

Published in
Advanced Materials Technologies

Citation (APA)
Ammu, S. K., Chen, X., Ulcay, D. G., Sharma, S., Alijani, F., Steeneken, P. G., Groen, P., & Masania, K. (2024). 3D Printing of Lead-Free Piezoelectric Ultrasound Transducers. *Advanced Materials Technologies*, *9*(23), Article 2400858. https://doi.org/10.1002/admt.202400858

ADVANCED MATERIALS TECHNOLOGIES
www.advmattechnol.de

3D Printing of Lead-Free Piezoelectric Ultrasound Transducers

*Satya K. Ammu, Xianfeng Chen, Derin Goulart Ulcay, Saurav Sharma, Farbod Alijani, Peter G. Steeneken, Pim Groen, and Kunal Masania**

Multi-material direct ink writing (DIW) of smart materials opens new possibilities for manufacturing complex-shaped structures with embedded sensing and actuation capabilities. In this study, DIW of UV-curable piezoelectric actuators is developed, which do not require high-temperature sintering, allowing direct integration with structural materials. Through particle size and ink rheology optimization, the highest $d_{33}{}^{*}g_{33}$ piezoelectric constant compared to other DIW fabricated piezo composites is achieved, enabling tunable actuation performance. This is used to fabricate ultrasound transducers by printing piezoelectric vibrating membranes along with their support structures made from a structural ink. The impact of transducer design and scaling up transducer dimensions on the resonance behavior to design millimeter-scale ultrasound transducers with desired out-of-plane displacement is explored. A significant increase in output pressure with increasing membrane dimensions is observed. Finally, a practical application is demonstrated by using the printed transducer for accurate proximity sensing using time of flight measurements. The scalability and flexibility of the reported DIW of piezo composites can open up new advancements in biomedical, human-computer interaction, and aerospace fields.

1. Introduction

Due to their accuracy, fast response, and energy efficiency, piezoelectric ultrasound transducers find extensive applications in haptic devices,[1] gesture detection,[2] and time-of-flight sensors.[3] Despite their broad potential, such devices made from silicon-based microfabrication techniques[4] remain bulky and planar, posing challenges for seamless integration into complex structures. The emergence of multi-material 3D printing[5] and functional materials offers new possibilities for the development of intelligent structures with embedded sensing and actuation capabilities.[6]

Among these technologies, direct ink writing (DIW) stands out for its ability to combine structural and sensing materials within the same printed object through ink design. DIW has been successfully used in fabricating soft electronics[7] and embedded sensors.[8] Currently, research on 3D-printed ultrasound transducers primarily focuses on piezoelectric ceramics that require high-temperature sintering.[9,10] Previous studies have demonstrated excellent piezoelectric properties of d_{33} from 388 to 496 pC N^{-1} achieved through DIW of piezoelectric ceramic-based transducers.[11] Nonetheless, the need for high-temperature sintering typically above 1000 °C, to densify the ceramic introduces risks of cracks and high porosity in the 3D printed parts and limits their direct integration with other structural materials.

S. K. Ammu, D. G. Ulcay, S. Sharma, K. Masania
Shaping Matter Lab
Faculty of Aerospace Engineering
Delft University of Technology
Delft 2629 HS, The Netherlands
E-mail: K.Masania@tudelft.nl

The ORCID identification number(s) for the author(s) of this article can be found under https://doi.org/10.1002/admt.202400858

[+]Present address: A*STAR Quantum Innovation Centre(Q.InC), Institute of Materials Research and Engineering (IMRE), Agency for Science, Technology and Research (A*STAR), 2 Fusionopolis Way, Innovis #08-03, Singapore 138634, Republic of Singapore

DOI: 10.1002/admt.202400858

X. Chen[+], F. Alijani, P. G. Steeneken
Department of Precision and Microsystems Engineering
Delft University of Technology
Mekelweg 2, Delft 2628 CD, The Netherlands

P. G. Steeneken
Kavli Institute of Nanoscience
Delft University of Technology
Lorentzweg 1, Delft 2628 CJ, The Netherlands

P. Groen
Novel Aerospace Materials
Delft University of Technology
Delft 2629 HS, The Netherlands

To address this high-temperature processing step, direct printing methods such as solvent evaporation-assisted 3D printing of piezoelectric poly(vinylidene fluoride) (PVDF) nanocomposites, allow for the creation of transducers that offer improved integration into structures.[12] However, this relies on printing using high amounts of solvents, which can lead to increased porosity. Although porosity can benefit sensing applications, it poses challenges for actuation applications due to lower mechanical stiffness, reduced block force, electrostatic breakdown, and poor electro-mechanical coupling efficiency. Further, PVDF and its co-polymers have poor temperature stability compared to piezo-ceramics and poor adhesion to other substrates, making integration into structures challenging.

Piezo ceramic-polymer composites are a promising alternative as they offer a favorable combination of good piezoelectric properties, high-temperature stability, low poling voltages, and the conformability and versatility of the polymeric continuous phase.[13] The piezoelectric properties of these composites are highly dependent on the volume fraction of the piezoelectric particles, with higher fractions leading to enhanced electro-mechanical coupling factors.[14] Despite the potential demonstrated by DIW of piezoelectric composites, current solutions are constrained by low volume fractions to mitigate nozzle clogging, limiting maximum piezoelectric performance to voltage generation for sensing or energy harvesting applications.[15,16]

Consequently, there is a need for a 3D printable piezo-composite system that can offer a combination of high piezoelectric response and seamless integration into structures. Here, we develop a method for direct ink writing of ultrasound transducers using a lead-free, 3% Li-substituted sodium potassium niobate $K_{0.485}Na_{0.485}Li_{0.03}NbO_3$ (KNLN), in combination with UV curable monomers. Potassium sodium niobate (KNN) has shown promise in terms of their piezoelectric properties,[17] biocompatibility[18] and have been demonstrated successfully to outperform both bulk PZT and most composites in sensing and energy harvesting applications.[19,20] To ensure both shaping freedom and piezoelectric performance, we propose to split these functions. Utilizing a multi-material 3D printing technique, we print a UV-curable piezoelectric vibrating membrane along with a support structure using structural ink. This method enables the printing and UV curing of piezoelectric ultrasound transducers without additional high-temperature sintering post-processes. By optimizing the composite properties, we can attain high piezoelectric properties while ensuring a robust bonding between the piezo materials and other structural materials. We perform finite element simulations to establish the design principles of these transducers and subsequently investigate their acoustic pressure generation and application in distance measurement. Our approach with DIW piezoceramic-polymer composites allows for the creation of ultrasound transducers with millimeter-scale dimensions using commercial 3D printers while providing flexibility in tailoring the transducer's mechano-acoustic properties such as freely tunable operating frequencies. This scalability and flexibility can benefit a wide array of applications in biomedical, structural, robotic interfaces, and energy fields.

2. Results and Discussion

Our approach to directly printed ultrasound transducers combines the 3D printing of a UV curable piezoelectric-composite ink that is optimized for its piezoelectric performance, along with a structural ink used for printing the clamping support for the piezoelectric membrane. The DIW process used to fabricate piezoelectric ultrasound transducers is shown in **Figure 1**. The piezoelectric ink consists of synthesized KNLN micro-particles (Figure S1a, Supporting Information) that are dispersed in a UV-curable monomer, poly(ethylene glycol) diacrylate, PEGDA-250 (Figure S1b, Supporting Information). The ink's piezoelectric and rheological properties are optimized for actuation while ensuring compatibility with DIW and co-curing with structural materials. First, the piezoelectric membrane is fabricated through a layer-by-layer extrusion process of the piezo ink, followed by sequential UV curing of each layer. This sequential curing ensures adequate UV penetration and curing in the piezo layers, resulting in structural integrity. Next, a structural ink comprising UV-curable PEGDA-250 with fumed silica is used to print the membrane's supporting structure (Figure 1b), enabling radial clamping of the membrane and facilitating out-of-plane vibration. The resulting transducer is inverted after printing. The top and bottom electrodes are then integrated on to the transducer either by gold sputtering or by painting using a conductive carbon paste. This is followed by a poling process to align the piezoelectric domains within the material, as explained in the Experimental Section. Figure 1c illustrates the functioning of the poled transducer, depicting the application of input voltage and the resultant ultrasound pressure generated from the output vibration. This allows for directly printed and UV-cured ultrasound transducers, allowing functional material integration into structures which is conceptualized in Figure 1d.

2.1. Optimization of Printing and Functional Properties of Piezo and Structural Inks

We first study the printing and electro-mechanical properties of the piezoelectric ink and the supporting ink followed by the design of the ultrasound transducers using these inks. The piezoelectric properties of particle-based piezo composites are significantly influenced by the volume fraction of the filler, with a higher fraction leading to higher piezoelectric constants and better electro-mechanical coupling factors.[14] To ensure efficient functioning in both actuation and sensing applications, it is crucial to maximize the volume fraction of the piezoelectric particles in the ink while maintaining compatibility with DIW process. Therefore, we investigated the influence of KNLN particle size on the maximum volume fraction and resulting printing properties and piezoelectric coefficients of the ink when used in DIW. Since the direct ink writing setup uses rheologically engineered inks that undergo a reversible viscoelastic transition in response to shear forces, one of the critical factors to consider is the influence of particle size on the ability of the ink to undergo an elastic to viscous transition on the application of shear and then recover to a weakly flocculated elastic structure on the removal of shear forces. This elastic recovery is governed by the Brownian forces that randomize the particles suspended in the ink and

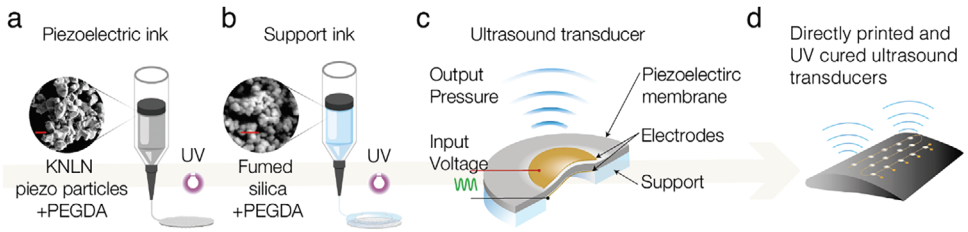

Figure 1. Direct ink writing (DIW) of UV-curable piezoelectric ultrasound transducers. (a) DIW process for printing the piezoelectric membrane using a KNLN microparticle-based ink, followed by UV curing. The inset shows the scanning electron microscope (SEM) image of the KNLN particles (red scale bar, 2 μm). (b) Printing of the support structure that clamps the piezoelectric membrane using a support ink containing fumed silica mixed with UV-curable PEGDA. The inset shows the SEM image of the fumed silica particles (scale bar, 200 nm). (c) Cross-sectional representation of the ultrasound transducer, along with top and bottom electrodes. Schematic demonstrates the working principle, indicating the input AC voltage and the resulting ultrasound pressure due to the output vibration of the piezoelectric membrane. (d) Directly printed and UV-cured ultrasound transducers enable the creation of intelligent structures with embedded transducers.

create a weakly interconnected network, thus allowing the ink to support its weight and subsequent layers against gravity and capillary forces, ultimately leading to freestanding 3D shapes.

The ratio of gravitational to Brownian forces is proportional to:[21]

$$\frac{Grav}{Brownian} \propto \frac{a^4 \Delta\rho g}{k_B T} \quad (1)$$

where a is the radius of the particle or clump of particles, $\Delta\rho$ is the difference in density between the particle and the liquid medium, $g = 9.8\ \mathrm{m\ s^{-2}}$ is the acceleration due to gravity, $k_B = 1.38{\times}10^{-23}$ $\mathrm{J{\cdot}K^{-1}}$ is the Boltzmann constant and, T = Temperature in K

Based on this equation, inks containing larger particles experience increased sedimentation and phase separation due to the power law growth in gravitational forces with particle size ($\propto a^3$) compared to the Brownian forces that randomize the particles, as depicted in **Figure** 2a (black line). From Equation (1), we calculated the critical size for KNLN particles to undergo sedimentation in the PEGDA medium to be 0.6 μm (Table S1, Supporting Information). Well-distributed particles smaller than 0.6 μm are preferable for direct ink writing as they quickly recover their randomized network structure after printing, enabling good shape retention and the creation of complex geometries.

Conversely, smaller, sub-micron particles exhibit significantly greater surface area relative to their volume ($\propto a^{-1}$), as illustrated by the surface area to volume ratio in Figure 2a (blue line). The increase in surface area results in higher inter-particle interactions and faster network jamming, thus increasing viscosity and limiting the maximum volume fraction. Therefore, we hypothesize that depending on the particle size used in the composite, a trade-off emerges between printability governed by the ink recovery and the piezoelectric properties determined by the maximum printable volume fraction, and this trade-off needs to be optimized particularly in applications that demand high electromechanical performance.

To further explore this trade-off in the KNLN-PEGDA system and determine the dominant parameter, two sets of KNLN particles with sizes approximating these critical values were synthesized with varying milling durations, as shown in Figure 2b. We synthesized KNLN particles using a two-step solid-state reaction further described in the Materials and Methods section, followed by either a 15-min ball milling process that resulted in an average particle size of 3.01 μm or ball milling for 20 h, leading to smaller particles with an average size of 0.87 μm (Figure 2b). The sizes of the synthesized particles are close to the theoretically calculated limits, as indicated by the highlighted regions in Figure 2a,b, allowing for assessing the trade-off between network recovery for printing and high piezoelectric performance.

The influence of particle size on the maximum achievable printable volume fraction was investigated by analyzing the successful viscoelastic transition of the inks when subjected to shear stress, as demonstrated in Figure 2c through oscillatory shear sweep tests. When using larger particles (3.01 μm), we observed that the maximum usable volume fraction with our desktop extrusion-based printer equipped with a 0.58 mm nozzle was 47.5%. At this volume fraction, the ink transitioned from elastic to viscous behavior at ≈50 Pa, indicated by the cross-over between the storage and loss moduli in the oscillatory shear stress sweep (Figure 2c). Beyond this volume fraction (>47.5%), the storage modulus and viscosity of the material, as shown in Figure S2a,b (Supporting Information), were too high and impeded smooth line printing, leading to issues with flow initiation and nozzle clogging. In contrast, when employing smaller particles (0.87 μm), the maximum printable volume fraction was limited to 25%, as shown in Figure 2c. This variation in the maximum usable volume fraction aligns with the hypothesis that larger particles, with their smaller surface area to volume ratio, experience fewer interparticle interactions. This results in reduced particle jamming compared to smaller particles and lower viscosity, thus allowing for an increased maximum printable volume fraction. This observation is consistent with literature on colloidal processing of other ceramics.[22]

Next, we conducted recovery tests that simulated the printing conditions to assess the viscoelastic recovery behavior of the inks after printing (Figure 2d). The ink containing smaller particles showed a quick drop in viscosity on being subjected to rotational shear stress followed by a rapid elastic recovery after removal of the stress, with the elastic shear modulus (solid squares) recovering almost instantly to original values, as seen in Figure 2d. In contrast, we observed that the ink with larger particles showed no recovery due to the increased gravitational forces compared to Brownian forces, which hinder the recovery of a network structure. This can be seen in Figure 2d, where the viscous part, G″ (hollow circles), demonstrates higher stress values than the elastic part, G′ (solid circles).

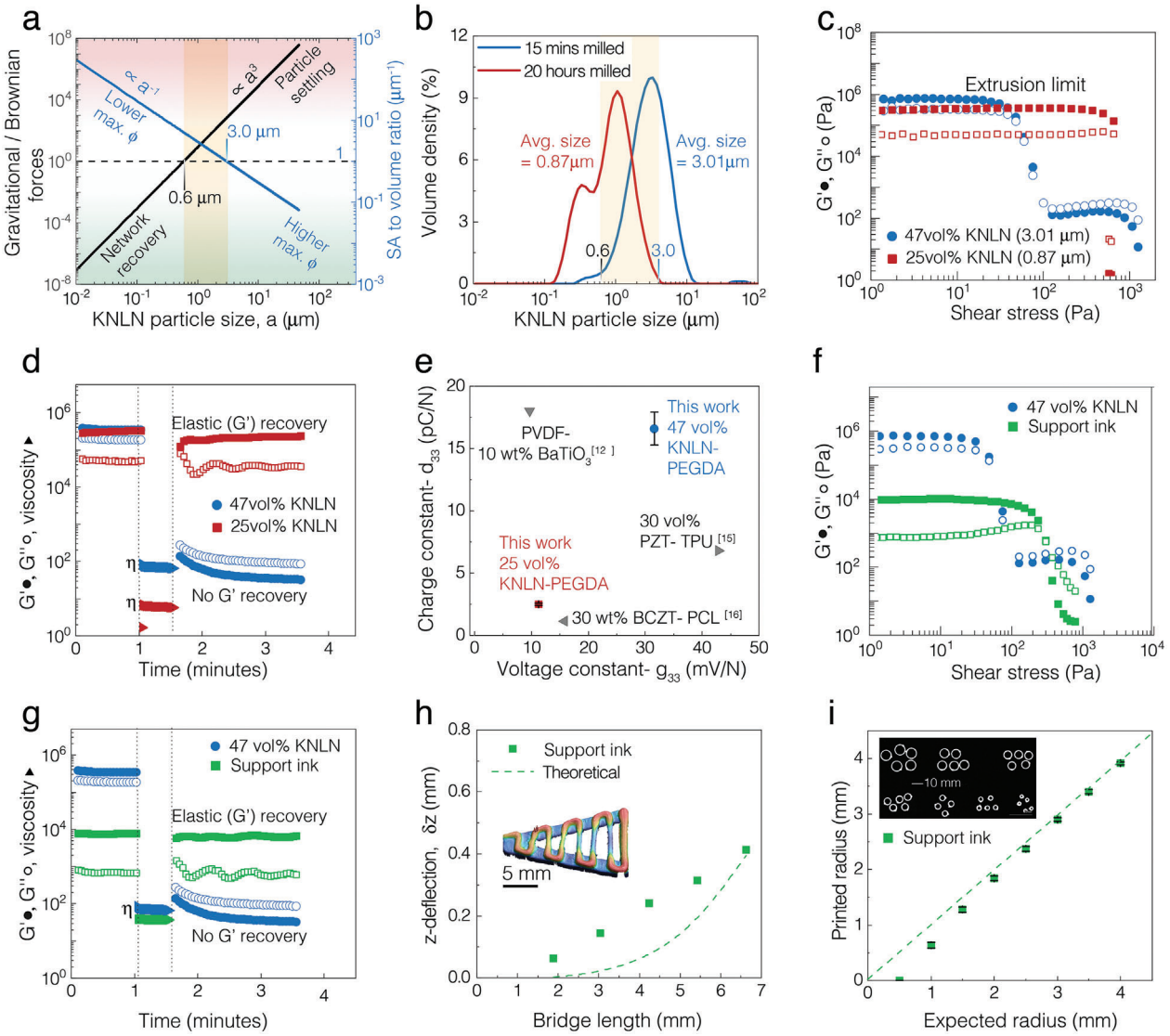

Figure 2. Printing and functional properties of the DIW inks for printable ceramic-polymer transducers. (a) Effect of particle size- *a* on the ratio of gravitational to Brownian forces (black line) versus ratio of surface area to volume (blue line) and their impact on physical phenomena relevant to printing and piezoelectric properties. The highlighted area between 0.6 and 3.0 μm denotes the region of interest in particle size where a trade-off occurs between those above two competing effects. (b) As highlighted, the particle size analysis of the synthesized KNLN powder under different milling conditions resulted in two distinct median particle size distributions close to the calculated critical particle size. (c) Impact of particle size on maximum storage and loss moduli (G′ and G″) and the resultant maximum extrudable volume fraction of the ink for varying particle sizes. (d) Evaluation of the elastic recovery behavior of the ink after shear tested via oscillation-rotation-oscillation test showing rapid elastic recovery for small particles and no recovery for the larger particles. (e) Piezoelectric properties of ink containing larger particles and a higher volume fraction (47 vol%) surpass state-of-the-art extrusion-based sintering-free piezo-composites. (f) Oscillatory shear sweep of support ink created for printing the support structures. (g) The recovery test of the support ink shows quick elastic recovery compared to the piezo ink. (h) Bridging test evaluating the sagging behavior with the length of the bridging element for the support ink. The inset shows the optical microscope image of the bridging test. (i) Assessment of dimensional accuracy of the diameters of the support structure, exhibiting close agreement with theoretical values and high repeatability above 1 mm as indicated by the low standard deviation ($n = 5$). The inset shows the image of the printed support structures with varying diameters.

Whilst this presents a problem for printing relying on the recovery of yield stress to provide fidelity, this lack of recovery of elastic properties in the ink with larger particles can be effectively addressed by in-situ curing of a UV-curable monomer sequentially before printing succeeding layers of ink. The in-situ UV curing of the composite ink leads to a highly cross-linked and stiff polymer matrix with a Tg ≈75 °C (Figure S3a, Supporting Information) and significantly increases the yield strength to ≈2.1 kPa, compared to the 50 Pa of the uncured ink, as depicted in Figure S3b (Supporting Information), allowing it to achieve sufficient yield strength to resist the weight imposed by subsequent layers and prevent gravitational sagging.

Lastly, we examined how particle size and their resulting volume fractions influence the piezoelectric performance of the two inks. The ink with smaller particles with a volume fraction of 25% has a d_{33} of 2.5 pC. N^{-1} and g_{33} of 11 mV.N^{-1}, and is

consistent with state-of-the-art DIW piezo-composite formulations with similar volume fractions.[16] However, the ink with larger particles exhibits significantly higher d_{33} of 17 pC. N^{-1} and g_{33} of 32 mV.N^{-1}, particularly a much greater d_{33} than the smaller particle ink, as shown in Figure 2e.

This difference in properties between the two particle sizes is mainly attributed to the dominance of volume-related effects when using larger particles. Based on Yamada's model[14] for binary systems with piezoelectric ceramic fillers distributed in a polymer, we know that the dielectric constant of the composite is highly dependent on the dielectric constant of the polymer matrix. Particularly in composites with significant differences in dielectric constant between the filler and matrix, the applied electric field gets confined by the low dielectric permittivity of the polymer and is unable to transfer effectively to the filler.[19] Hence, previous work by Stuber et al. has observed that larger particles and agglomerations can increase the dielectric constant, likely due to the lower amount of filler-matrix interfaces.[23] In essence, anything that reduces the mismatch between the permittivity of the filler and matrix, or reduces the number of interfaces where these losses can occur, can help in increasing the piezoelectric properties of the composite.

Using larger particles leads to lower interfacial effects, which primarily contributes to reduced viscosity at higher volume fractions, while also reducing dielectric losses at the interface between the high dielectric constant piezoelectric filler and low dielectric constant matrix. Consequently, this leads to significantly higher dielectric and piezoelectric constants for the larger particles.

These findings align with the analytical predictions made for these piezo-composites utilizing randomly dispersed particles, as shown in Figures S5–S7 (Supporting Information). This combination of both high d_{33} and g_{33} values for the KNLN ink with larger particles compared to other DIW piezoelectric materials, as shown in Figure 2e, makes the ink suitable for transducer devices capable of operation in both actuation and sensing modes. This, however, comes at the expense of poor elastic recovery after printing due to increased gravitational forces, which we resolved by sequentially UV-curing each layer (Figure S3b, Supporting Information).

Further, a support ink was developed to print the non-piezoelectric support precisely, clamping the piezoelectric membrane and facilitating its vibrational movement. The support ink was formulated by incorporating 8 wt.% hydrophobic fumed silica into PEGDA. Rheological characterization of the support ink, as shown in Figure 2f, demonstrated that the support ink undergoes a similar viscoelastic transition on the application of shear forces compared to the piezoelectric ink, as seen by the crossover of the storage and loss moduli (G′ and G″). The elastic recovery of the support ink was tested similarly to the piezo inks and it can be seen that they exhibit immediate elastic recovery upon removal of shear stress (Figure 2g) as seen by the instantaneous recovery of the storage moduli (G′) after removal of rotational shear. This enables printing support structure layers successively without the need for intermediate curing, as they can retain their shape through elastic recovery and support subsequent layers due to their high elastic properties.

The load-bearing capabilities of the support ink are essential as they serve the critical role of forming the clamping piezoelectric structure. Prints were evaluated by examining the sagging of bridging elements printed with this ink. The results demonstrated that the ink effectively bridged spans of up to 3.5 mm with minimal sagging, maintaining a tolerable sag of less than 0.2 mm. Additionally, the extent of sagging (z-deflection) in the printed filaments increased proportionately to the spanning length, as depicted in Figure 2i. We hypothesize that the difference in measured versus theoretical deflection, especially for shorter spanning lengths, arises from the viscoelastic nature of the material and due to the shear-thinning nature of the paste. Smaller aspect ratio beams tend to experience more shear-induced deformation, as predicted by Timoshenko's beam theory[24] and for aspect ratios smaller than five, beam theories become inaccurate. As the aspect ratio increases, the experimental results increasingly match the Euler-Bernoulli predictions as seen in Figure S4 (Supporting Information), showing that lower aspect ratio beams are significantly influenced by shear deformation.

Since the operating parameters such as frequency and out-of-plane displacement of the piezo membranes also depend on the geometry and clamping efficiency of the support structure, it is important to test the precision in printing of support structure inks. The precision of the support structure was examined by printing circular rings and subsequently measuring the printed diameters. When attempting to print a ring with an inner radius of 0.5 mm, the printed ring gets filled and closed. This may result from a combination of factors, including the nozzle diameter being the same size as the print radius and the viscoelastic material properties leading to extensional effects, cohesion and closing of small gaps. However, from 1.5 mm radius onward, we identified that reliable prints could be achieved with a nozzle with a diameter of 0.58 mm, as evidenced by low standard deviation values in Figure 2h.

The optimized piezoelectric ink and support inks were subsequently utilized to print and test ultrasound transducers.

2.2. Design and Dynamic Characterization of the 3D Printed Ultrasound Transducers

We then utilize the optimized piezoelectric and support inks to print ultrasound transducers and characterize their dynamic behavior. Circular piezoelectric membranes with radius (r) and thickness (t) were 3D printed, along with a support structure of constant height (0.6 mm) and wall thickness (S = 1.1 mm) to clamp the membrane (**Figure 3**a; also Figure S8, Supporting Information). The mechanical vibrations of the piezo membranes with electrical input were measured using a Polytec Laser Doppler Vibrometer (LDV), as shown in Figure 3a (also Figure S9, Supporting Information for actual setup and printed transducers). In order to understand the frequency-dependent dynamic behavior of the membranes, a linear chirp signal generated by the LDV function generator was used to stimulate the membranes and the resulting out-of-plane displacement was measured. Figure 3b presents the area-averaged magnitude of the frequency response of the transducer with r = 1.5 mm and t = 0.2 mm, showing three vibration modes. It is noted that the fundamental mode, observed as the first peak in the frequency response curve, exhibits the highest displacement. This mode

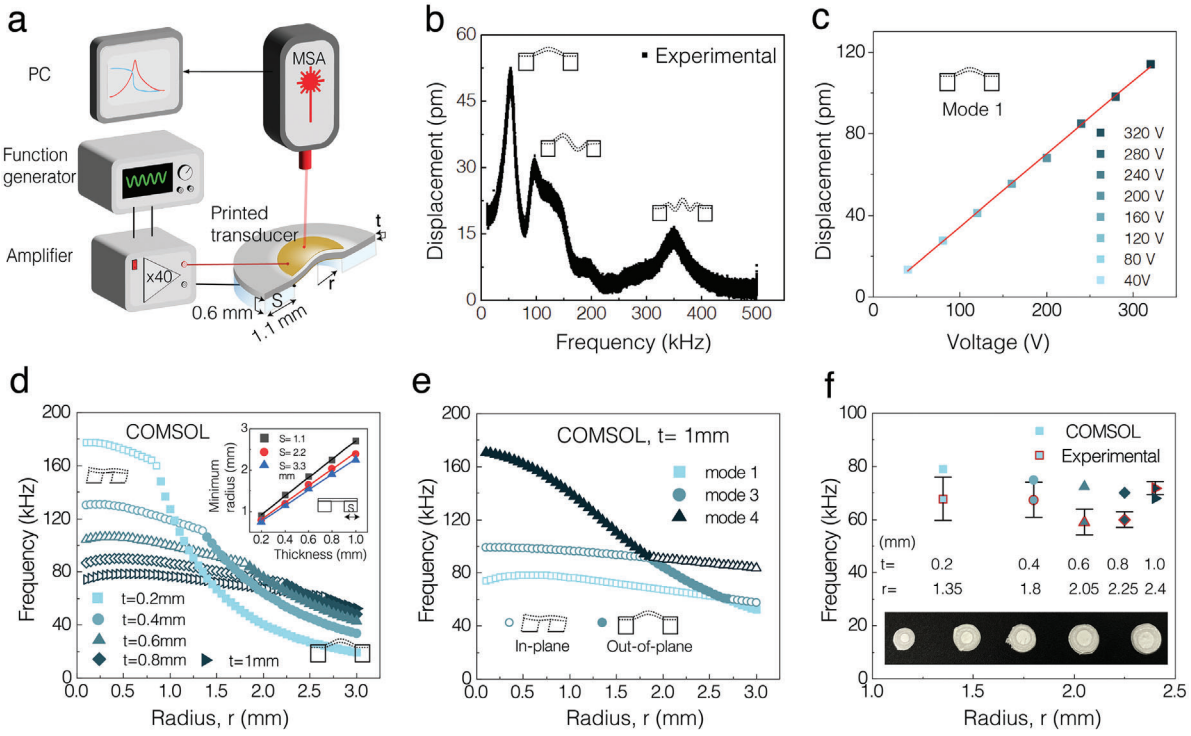

Figure 3. Design and dynamic characterization of the 3D printed ultrasound transducers. (a) Schematic of the setup, illustrating the printed transducer with a radius (r) and thickness (t), driven to resonance by a waveform function generator amplified by a 40x voltage amplifier. Membrane vibrations are measured using a Polytec Laser Doppler Vibrometer (LDV) MSA400. (b) Measured frequency response of a transducer with $r = 1.5$ mm and $t = 0.2$ mm, along with the corresponding schematics of mode shapes. The frequency response of the membrane shows maximum out-of-plane displacement in the fundamental mode. (c) The linear increase in the out-of-plane peak displacement amplitude of the first resonant mode with input voltage. (d) COMSOL simulation data illustrating the impact of varying radius (r) and thickness (t) of the transducer on the fundamental mode frequency and mode shape, highlighting the transition from in-plane displacement (hollow points) to out-of-plane (solid points) with increasing radius and decreasing thickness of the piezo-membrane. The inset indicates that for a specific support thickness S, the minimum radius of the membrane required to maintain the out-of-plane mode increases linearly with the thickness of the membrane. (e) Behavior of higher modes in thicker transducers ($t = 1$ mm) with varying radii. (f) Specific thickness (t) and radius (r) combinations were used for manufacturing to maintain a constant frequency. Experimental fundamental mode frequencies are compared to those obtained from COMSOL simulation, demonstrating close agreement.

corresponds to the axisymmetric out-of-plane bending motion of the piezo-membrane, enabling the membrane to act as a monopole source and efficiently radiate sound by voltage signal.

To understand the voltage-dependent actuation of this mode, we measured the frequency response of the membrane at a point near its center under different excitation voltages. To prevent the electrical and mechanical breakdown of the membranes, we operated the transducer at much lower voltages (max. 200 V) than the breakdown voltage (>2000 V). We observed that displacement increases linearly with increasing voltage, as indicated by the linear relationship between the out-of-plane displacement and the voltage in Figure 3c. This is beneficial for the linear tunability of the sound pressures when developing a sound transducer.

To leverage the capability of fabricating millimeter-scale ultrasound transducers, we investigated the impact of further increasing the transducer dimensions on the resonance behavior and out-of-plane motion of the membranes. Using finite element simulation with COMSOL, we analyzed the effect of changing the radius (r) and thickness (t) on the dynamic behavior of the membrane. In the simulations, we first derived the mechanical, dielectric, and piezoelectric properties of the 47 vol% KNLN-PEGDA piezo-composite from analytical methods and incorporated them into a custom material in the FEM model (Figures S5 and S6, Supporting Information). Then, the influence of changing dimensions of the piezo membrane on the mode shapes and resonance frequencies was analyzed, as shown in Figure 3d.

The analysis revealed that increasing the radius while decreasing the thickness of the membrane led to a transition in the fundamental resonance mode, shifting from primarily in-plane displacement (depicted by hollow points) to the desired out-of-plane motion (depicted by solid points) (Figure 3d). Simulations indicated that once the transducer shifted to the out-of-plane displacement mode, the fundamental frequency decreased exponentially with increasing radius, as expected, which is particularly evident for the $t = 0.2$ mm membrane (square points). To further investigate this, we examined the relationship between membrane thickness and the minimum radius required to have out-of-plane motion, illustrated in the inset, demonstrating a linear increase with thickness. This results in a constant ratio of thickness and radius (t/r) or slenderness of the membrane, as shown in the inset, allowing the piezo layer to vibrate as a membrane.

We also observed that changing the thickness of the support structure (S) affected this slenderness for the membrane mode, with increasing support thickness causing a reduction in the

minimum radius (inset of Figure 3d). However, we observed that further increase in support thickness have a diminishing effect when changing S from 2.2 to 3.3 mm. This shows that the support thickness also plays a role in the fundamental frequency of the transducers, particularly if the thickness is insufficient for effective clamping. The optimal support thickness where the effect of the support diminishes depends on the thickness of the membrane.

As discussed earlier, the minimum radius requirement increases with greater thickness. Therefore, we examined the displacement and mode shape of higher modes in thicker transducers (t = 1 mm) with varying radii, as depicted in Figure 3e. It can be seen that when the radii are less than 2.5 mm, the fundamental mode does not exhibit the desired out-of-plane mode, but mode shape with complex bulk motion, since the resonator cannot be taken as a simple plate or membrane. However, to maximize the output sound pressure and transduction efficiency when designing a sound transducer, it is preferable to have the out-of-plane mode as the fundamental mode and higher-order modes such as mode 3 (1.75 < r < 2.5 mm) and mode 4 (r < 1.75 mm) demonstrate some out-of-plane displacement, as emphasized by the solid points.

By understanding how the dimensions of a 3D-printed transducer membrane and support impact its resonance behavior, we can create custom designs that deliver the desired frequency and displacement type. These insights were utilized to select specific thickness and radius combinations during the manufacturing process to maintain a nearly constant frequency, as illustrated in Figure 3f. The thickness of the transducer membranes was incrementally increased from 0.2 to 1.0 mm with a 0.2 mm step, aligning with the printing layer height. To maintain a consistent frequency and mitigate the impact of frequency variations on the measured pressure, given that sound attenuation is frequency-dependent, specific radii were chosen for these thicknesses to maintain a nearly constant frequency throughout the samples.

To validate our findings, we compared the experimentally measured fundamental frequencies with the frequencies predicted by our model. We observed that the experimental measurements agree well with the simulations (Figure 3f), with slightly lower magnitudes, likely attributed to imperfect clamping conditions (Figure S10a,b, Supporting Information). Further, analyzing the standard deviation (SD) of the resonant frequency measurements (n > 4) indicates reduced variation for larger transducers. This higher accuracy with larger transducers demonstrates the advantage of DIW of transducers, as it allows for the fabrication of transducers with larger thickness values compared to SOI-based transducers, allowing commercial 3D printing techniques to be utilized without the need for micro-scale precision, showing the practical applicability of the fabrication process.

2.3. Sound Pressure Measurement and Application of 3D Printed Ultrasound Transducers

We then characterize the sound pressure generated by the 3D-printed ultrasound transducers using the experimental setup as shown in **Figures** 4a and S11 (Supporting Information). By driving the printed transducer to resonance using a sine wave voltage signal, ultrasound was generated through the membrane's vibrations and then captured by a commercial wide-spectrum ultrasound microphone M500. This microphone M500 gave us relative pressure values, which were then calibrated using a commercial Murata 40 kHz ultrasound transducer with a known output sound pressure to convert relative pressure to absolute values, as detailed in Supporting Information (Figure S12, Supporting Information). Further, we used a conductive grounding plane between the printed transducer and the microphone to eliminate any electromagnetic interference and ensure only the measurement of the transducer's acoustic output.

Figure 4b shows the pressure and frequency of the generated ultrasound at various input voltages, as captured by the microphone. Notably, we observed a linear relationship between the output sound pressure and the input voltage (see the inset of Figure 4b), which shows the advantage of scaling up to millimeter-scale dimensions, as higher input voltages can be applied without electrical breakdown, resulting in higher output pressures. Figure 4c illustrates the relationship between this generated sound pressure and the distance of measurement, exhibiting a decay in the far-field zone beyond 5 cm. While the sound pressure measurements in the near-field zone (<5 cm) were affected by constructive and destructive interference from reflected waves, the far field (>5 cm) provides a conducive environment for precise sound pressure measurements using a single microphone setup[25] as interference from reflected waves can be minimized. Consequently, all pressure measurements were conducted at this optimal distance.

To underscore the significance of transducer size on the generated output pressure, we measure the sound pressures of transducers with varying radius and thickness combinations, as presented in Figure 4d. As can be seen in Figure 4d, enlarging the transducer size from (t,r) = (0.2,1.35) to (0.4,1.8) mm results in a substantial increase in the mean output pressure from 0.21 to 0.63 Pa. This shows the significance of creating ultrasound transducers with larger dimensions, enabling the fabrication of transducers with mm-scale dimensions using commercial 3D printers.

With further increases in dimensions, particularly observed for t = 0.6,0.8, and 1 mm, it becomes evident that while the net pressure continues to rise, the rate of increase diminishes with larger dimensions. This trend can be explained by the diminishing clamping efficiency of the support structure as thickness increases while maintaining the same support thickness. This results in the inefficient higher-order modes becoming increasingly proximal to the efficient out-of-plane displacement modes as thickness grows (Figure S10b, Supporting Information). Consequently, multiple modes are activated, resulting in lower output pressure than anticipated.

To demonstrate the actuation capability and show the 3D printed transducer as an ultrasound actuator for distance measurement, a 40 kHz transducer was designed based on the guidelines obtained from previously described simulations and 3D printing (Figure S13, Supporting Information). This printed transducer was then actuated using a sinusoidal voltage signal at the same frequency. A commercial 40 kHz Murata ultrasound transducer was used as the receiver. The Time of Flight (ToF), as shown in Figure 4e, between the transmitted and received signals was utilized to calculate the measured distance between the actuator and the receiver. Measurements with distance below 40 mm were unreliable due to interference from the near field

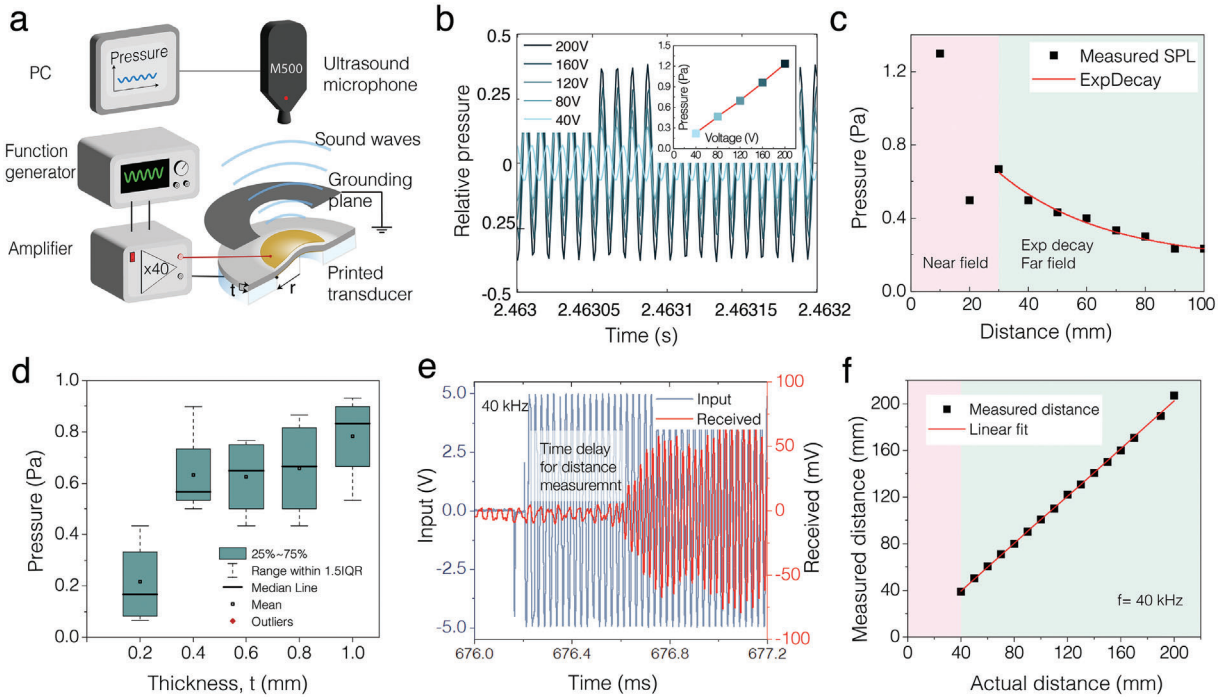

Figure 4. Sound pressure measurement and application of 3D printed ultrasound transducers. (a) Schematic of the sound pressure measurement setup testing the actuation mode of the printed transducer, illustrating the sound generation upon application of input voltage signal and measured pressure. A grounding plane eliminates electromagnetic interference between the microphone and the 3D-printed transducer, ensuring the measurement of sound pressure without interference. (b) The signal measured by the microphone shows the pressure and frequency of the generated ultrasound at different input voltages. The inset shows the linear increase in output sound pressure with rising input voltage. (c) Sound pressure versus distance, displaying a power-law decay in the far-field zone from 5 cm. (d) Sound pressure measurements for transducers with different radius and thickness combinations at comparable operating frequencies, illustrating that increasing the transducer size, though not linearly, enhances output pressure. (e) Time of Flight (ToF) is measured using the emitted signal from the 3D-printed transducer as an ultrasound transmitter and the received signal from a commercial transducer for distance measurement. (f) The comparison between measured and actual distances showed good agreement between distances of 40 and 200 mm.

and electromagnetic interference, obscuring the first peak and potentially resulting in miscalculations. Additionally, distances above 200 mm could not be measured, as they exceeded the height limit of the printer used to set the distance between the actuator and the commercial sensor. The measured distances obtained from ToF using the 3D printed transducers exhibited excellent agreement with the actual distances within the range of 40–200 mm as can be seen in Figure 4f. This highlights the practicality and versatility of the 3D printed transducers, emphasizing the ease with which they can be printed and fine-tuned for diverse applications that demand actuation.

3. Conclusion

By optimizing particle size and transducer design, we demonstrated tunable actuation performance in 3D-printed piezoelectric composites. We designed the piezo ink through careful selection of particle size to balance the trade-off between high piezoelectric response and the printing fidelity arising from competing effects of Brownian recovery and gravitational settling. Our examination of particle sizes revealed that larger particles ≈3 μm increase the d_{33} of the composite more than an order of magnitude than similar state-of-the-art direct ink writing piezo composites. The loss of the elastic recovery of the ink due to the increased size of particles was effectively addressed by an in-situ layer-by-layer curing of the UV-curable piezo ink. This enabled us to create free-form piezoelectric materials that can be co-cured with structural materials at room temperature to create ultrasound transducers with a tailorable frequency response.

Further, we studied the impact of scaling up transducer dimensions on membrane resonance behavior to design millimetre-scale ultrasound transducers with a desired out-of-plane motion. We tested the printed transducers at ≈80 kHz for the acoustic pressure generated through piezoelectric membrane vibration. The measurements revealed a significant increase in pressure with increasing transducer size, with an increase from (t,r) = (0.2,1.35) to (0.4,1.8) mm, resulting in a rise in mean output pressure from 0.21 to 0.63 Pa. Finally, we tuned the printed transducer to a frequency of 40 kHz and used it as a transmitter for precise and accurate distance measurement, showcasing the practical utility of our printed transducers.

In contrast to conventional silicon-based manufacturing, which requires microscale precision and high-temperature methods, our DIW-printed piezo composites using commercial 3D printers enable cost-effective mass printing of transducers into complex-shaped objects while ensuring robust bonding between the surfaces, opening up avenues in the field of multi-material 3D printing using functional materials. Thus, our printing

technique provides a pathway to scalable and bio-compatible manufacturing of piezo-embedded intelligent structures with built-in sensing and actuation capabilities, with potential applications in the field of bio-medical devices and aerospace engineering.

4. Experimental Section

Ceramic Synthesis: $K_{0.485}Na_{0.485}Li_{0.03}NbO_3$ (KNLN) ceramic powder was prepared through a conventional solid-state reaction with a two-step calcination procedure that has been previously studied.[26] Stoichiometric proportions of >99% Na_2CO_3, K_2CO_3, Li_2CO_3, and Nb_2O_5 (Sigma–Aldrich) were milled with 5 mm yttria-stabilized ZrO_2 balls in hexane for 3 h at 200 rpm. The milled powders were air dried on a hot plate at 100 °C for 1 h, and the dried green powder was calcined at 1050 °C for 3 h with a heating rate of 5 °C min^{-1}. The calcined ceramic was milled with 5 mm balls in IPA for 3 h at 200 rpm, followed by air dying and a second, longer calcination at 925 °C for 20 h with a heating rate of 1 °C min^{-1}. The calcined powder was ball milled in IPA for 15 min, air dried, sieved through a 90 µm sieve, and then stored under vacuum. The particle morphology was analyzed using a Scanning Electron Microscope, SEM (JEOL, JSM-7500F, Nieuw Vennep, the Netherlands). The particle size distribution of the milled powders was measured using Malvern Mastersizer 3000 on 0.1% weight/volume aqueous solution of the powders using sodium dodecyl sulfate solution as surfactant. The mean value of the distribution then represented the particle size of each type of powder.

Ink Preparation—Piezoelectric Ink: The synthesized ceramic powder was mixed with the UV-sensitive monomer Poly (ethylene glycol) diacrylate with Mn 250 (Sigma–Aldrich) in varying volume fractions and combined in a planetary mixer (SpeedMixer DAC 150.1 FVZ) at 3500 rpm for 2 min in 30s intervals with a 15s break in between to prevent excessive heating of the components while high-speed mixing. Two photoinitiators (Irgacure 819, 184) were chosen to maximize the curing depth due to the high ceramic filler content to obtain a UV-curable piezoelectric ink. The photo-initiations were then added to the KNLN-PEGDA mixture in the ratio of 1% and 2% wt. with respect to the weight of the monomer and mixed at 1000 rpm for 5 min to ensure homogenous distribution of the initiators.

Ink Preparation—Support Ink: Eight weight percentage of hydrophobic pyrogenic fumed silica (HDK 18) wrt. to monomer weight was mixed with PEGDA 250 in a planetary mixer (SpeedMixer DAC 150.1 FVZ) at 3500 rpm for 5 min. Then, 1wt.% photoinitiator Irg 184 wrt to monomer weight was added to the mixture and mixed at 1000 rpm for 2 min.

Rheological Characterization: The rheological properties of the inks were characterized using a rotational rheometer (Haake Mars III, Thermoscientific) with a 20 mm diameter serrated plate geometry using a gap height of 1 mm. Serrated plates prevent artifacts in measurements arising from wall slip, which has been studied to occur when highly loaded dispersions are subject to high localized deformation. Shear storage and loss moduli were determined as a function of shear strain via dynamic amplitude sweeps at a fixed frequency of 1 Hz with a stress sweep. The yield stress was measured via steady-state flow experiments with a sweep of shear stress and measuring. The point of change in slope of the log–log plot of shear stress versus strain was used to calculate the yield stress of the ink. The elastic recovery of the ink was measured using a time-dependent oscillation-rotation-oscillation (ORO) test. To simulate at-rest behavior, an amplitude sweep was performed at low shear stress within the linear viscoelastic regime (LVR), followed by a high shear rate (10 s^{-1}) rotation to simulate the time scales and stresses experienced during printing. Subsequently, the recovery in elastic moduli over time was measured with the low amplitude oscillatory sweep.

Printing and Curing: A commercial desktop printer (Ultimaker 2+) was modified by replacing the original print head with a custom-made ink extrusion system consisting of a 25 mL syringe holder and a mechanically driven syringe pump. The 3D models of the transducers were sliced in Cura with a print speed of 10 mm s^{-1} using a nozzle with an inner nozzle diameter of 0.584 mm. The printed lines or parts were cured using an Omnicure S1500 (Lumen Dynamics) UV-lamp at 100% intensity at 20 cm for 2s between each layer and 10 s.for the final part

Bridging Ability of the Ink: To assess the ability of the support ink to be able to resist deformation under its weight and form complex shapes, a triangular support structure was printed like the work done by Kleger et al., followed by printing spanning filaments across the support structure. To evaluate the sagging behavior, the deflection of the filaments was imaged using a Keyence VR-5000 Optical Profilometer. The filaments' length and deflection were measured by analyzing the image from the Profilometer using ImageJ. The density of the support ink was measured to be 1.2 g cc. The storage modulus of the ink after recovery obtained from the recovery test was used to calculate the theoretical deflection. The experimental deflection was compared to the calculated theoretical deflection calculated in Section S5 (Supporting Information).

Poling: Depending on the application, either gold or carbon paste electrodes were applied. Gold electrodes were used for samples for LDV measurements to ensure a bright, reflective surface for the laser light. Gold electrodes (50–100 nm) were sputtered on the top of the transducer through a 3D-printed shadow mask with a sputter coater for 2 min (QuorumQ300T, East Sussex, UK). Since the gold electrodes were very thin and fragile, conductive carbon paste was obtained from Dupont 7102 and applied using a paintbrush for applications where robust electrodes were required without the need for high reflectivity. To align the dipoles in the piezoelectric domains, the piezo-composites were poled in a silicon oil bath kept at 120 °C by applying a DC field of 10 $kVmm^{-1}$ for 5 min. The electric field was then turned off, and the samples were retrieved immediately without cooling under the field and cleaned.

Piezoelectric Characterization: The piezoelectric charge coefficient, d_{33} (pC N^{-1}) of the poled piezoelectric films was measured using a Berlincourt (PM 300, Piezotest, London, UK) piezometer with a static force of 10 N and a dynamic peak-to-peak sinusoidal excitation of 0.25 N at 110 Hz. The capacitance and dielectric loss were measured at 1 kHz and 1 V with an Agilent 4263B LCR meter (Santa Clara, CA, USA). The value of relative permittivity ϵ_{33}, measured under zero stress, was derived from the capacitance. The piezoelectric voltage constant, g_{33} (mV m N^{-1}) of the films was calculated using the ratio of d_{33}/ϵ_{33}.

Laser Doppler Vibrometry: A Polytec Laser Doppler Vibrometer MSA400 was used for the dynamic behavior measurements. Signals were generated by the Polytec function generator and then amplified 40x (voltage gain) by a voltage amplifier (Delta Elektronica) to actuate the printed piezo transducer into vibration. The laser was generated by the MSA400 laser head and focused on the region of interest to read out the membrane's vibration signals, which will be subsequently decoded by a Polytec VD-09 Digital Velocity Decoder and transformed into digital velocity data.

Ultrasound Pressure: Sinusoidal voltage signals were generated by a function generator (33500B, Agilent Technologies, Loveland Colorado, USA) and then amplified 40x (voltage gain) by a voltage amplifier to actuate the printed piezo transducer into vibration. A commercial M500 USB Ultrasound microphone was used to receive the ultrasound, and the reading was obtained from the software Batsoundlite. The microphone was mounted to an Ultimaker head, and the printed transducer was placed on the bed. The gantry system of the Ultimaker was used as a precise x,y, and z-control stage to ensure the centering of the transducer and height measurement.

Distance Measurement: A 3D printed transducer, resonating primarily at 40 kHz, was fabricated and poled using the previously described method. Sinusoidal voltage signals were generated by a function generator (33500B, Agilent Technologies, USA) and amplified by 40x using a voltage amplifier (Delta Elektronica) to drive the printed piezo transducer into vibration. A commercial 40 kHz Murata ultrasound transducer received the ultrasound signals, and readings were captured using an oscilloscope (Picoscope 5442D). The receiver was attached to the head of a Prusa MK3 3D printer, while the printed transducer was positioned on the bed. The Prusa gantry system provided precise x, y, and z-control to ensure transducer alignment and height consistency. Continuous measurements were conducted using the Picoscope, and the input to the printed transducer was toggled manually to create a long pulse. The receiver output signal was amplified 40x and recorded through the oscilloscope. The amplitude

of the received signal takes some time to reach a stable level, and the first few waves have an amplitude lower than that of the electromagnetic noise. This makes it challenging to measure the time of flight using the first peaks; to combat this, it was observed that at a distance of 100 mm, the first trough with amplitude above the noise level corresponded to the fourth trough of the input signal. All other time of flight measurements were made consistently between the first trough of the received signal with amplitude above noise amplitude and the fourth trough of the transmitter input signal.

Supporting Information

Supporting Information is available from the Wiley Online Library or from the author.

Acknowledgements

S.S. and K.M. are funded by the European Union (ERC CoG, AM-IMATE, 101088968).

Conflict of Interest

The authors declare no conflict of interest.

Data Availability Statement

The data that support the findings of this study are available from the corresponding author upon reasonable request.

Keywords

additive manufacturing, direct ink writing, piezo-composites, ultrasound transducers

Received: June 19, 2024
Published online:

[1] K. Harrington, D. R. Large, G. Burnett, O. Georgiou, presented at *Proc. - 10th Int. ACM Conf. Automot. User Interfaces Interact. Veh. Appl. AutomotiveUI* Sep **2018**, 11.
[2] J. Yan, X. Yang, X. Sun, Z. Chen, H. Liu, *IEEE Sens. J.* **2019**, *19*, 5895.
[3] G. Gibbs, H. Jia, I. Madani, *Procedia* **2017**, *28*, 173.
[4] G.-L. Luo, Y. Kusano, D. A. Horsley, *J. Microelectromechanical Syst.* **2021**, *30*, 81.
[5] M. A. Skylar-Scott, J. Mueller, C. W. Visser, J. A. Lewis, *Nature* **2019**, *575*, 330.
[6] M. Wehner, R. L. Truby, D. J. Fitzgerald, B. Mosadegh, G. M. Whitesides, J. A. Lewis, R. J. Wood, *Nature* **2016**, *536*, 451.
[7] A. D. Valentine, T. A. Busbee, J. W. Boley, J. R. Raney, A. Chortos, A. Kotikian, J. D. Berrigan, M. F. Durstock, J. A. Lewis, *Adv. Mater.* **2017**, *29*, 1703817.
[8] J. T. Muth, D. M. Vogt, R. L. Truby, Y. Mengüç, D. B. Kolesky, R. J. Wood, J. A. Lewis, *Adv. Mater.* **2014**, *26*, 6307.
[9] Y. Zeng, L. Jiang, Y. Sun, Y. Yang, Y. Quan, S. Wei, G. Lu, R. Li, J. Rong, Y. Chen, Q. Zhou, *Micromachines* **2020**, *11*, 713.
[10] H. Lu, H. Cui, G. Lu, L. Jiang, R. Hensleigh, Y. Zeng, A. Rayes, M. K. Panduranga, M. Acharya, Z. Wang, A. Irimia, F. Wu, G. P. Carman, J. M. Morales, S. Putterman, L. W. Martin, Q. Zhou, X. (Rayne) Zheng, *Nat. Commun.* **2023**, *14*, 2418.
[11] J. E. Smay, J. Cesarano, B. A. Tuttle, J. A. Lewis, *J. Am. Ceram. Soc.* **2004**, *87*, 293.
[12] S. Bodkhe, G. Turcot, F. P. Gosselin, D. Therriault, *ACS Appl. Mater. Interfaces* **2017**, *9*, 20833.
[13] J. Holterman, P. Groen, *An introduction to piezoelectric materials and applications, Stichting AppliedPiezo*, **2013**.
[14] T. Yamada, T. Ueda, T. Kitayama, *J. Appl. Phys.* **1982**, *53*, 4328.
[15] R. Tao, J. Shi, F. Granier, M. Moeini, A. Akbarzadeh, D. Therriault, *Appl. Mater. Today* **2022**, *29*, 101596.
[16] Z. M. Tsikriteas, R. A. Heylen, S. Jindal, E. Mancuso, Z. Li, H. Khanbareh, *Adv. Mater. Technol.* **2023**, *8*, 2202127.
[17] Y. Saito, H. Takao, T. Tani, T. Nonoyama, K. Takatori, T. Homma, T. Nagaya, M. Nakamura, *Nature* **2004**, *432*, 84.
[18] N. H. Gaukås, Q. S. Huynh, A. A. Pratap, M. A. Einarsrud, T. Grande, R. M. D. Holsinger, J. Glaum, *ACS Appl. Bio Mater.* **2020**, *3*, 8714.
[19] D. B. Deutz, N. T. Mascarenhas, J. B. J. Schelen, D. M. de Leeuw, S. van der Zwaag, P. Groen, *Adv. Funct. Mater.* **2017**, *27*, 1700728.
[20] V. L. Stuber, D. B. Deutz, J. Bennett, D. Cannell, D. M. de Leeuw, S. van der Zwaag, P. Groen, *Energy Technol.* **2019**, *7*, 177.
[21] R. G. Larson, *The Structure and Reology of Complex Fluids*, Oxford University Press, New York **1999**.
[22] G. Tarì, J. M. F. Ferreira, A. T. Fonseca, O. Lyckfeldt, *J. Eur. Ceram. Soc.* **1998**, *18*, 249.
[23] V. L. Stuber, T. R. Mahon, S. van der Zwaag, P. Groen, *Mater. Res. Express* **2020**, *7*, 015703.
[24] C. M. Wang, J. N. Reddy, K. H. Lee, *Shear Deform. Beams Plates*, Elsevier, Amsterdam/New York **2000**, 11.
[25] S. F. Siemens, *Free versus Diffuse Field, Near versus Far Field*, https://community.sw.siemens.com/s/article/sound-fields-free-versus-diffuse-field-near-versus-far-field **2020** (accessed: January 2024).
[26] N. K. James, D. B. Deutz, R. K. Bose, S. van der Zwaag, P. Groen, *J. Am. Ceram. Soc.* **2016**, *99*, 3957.